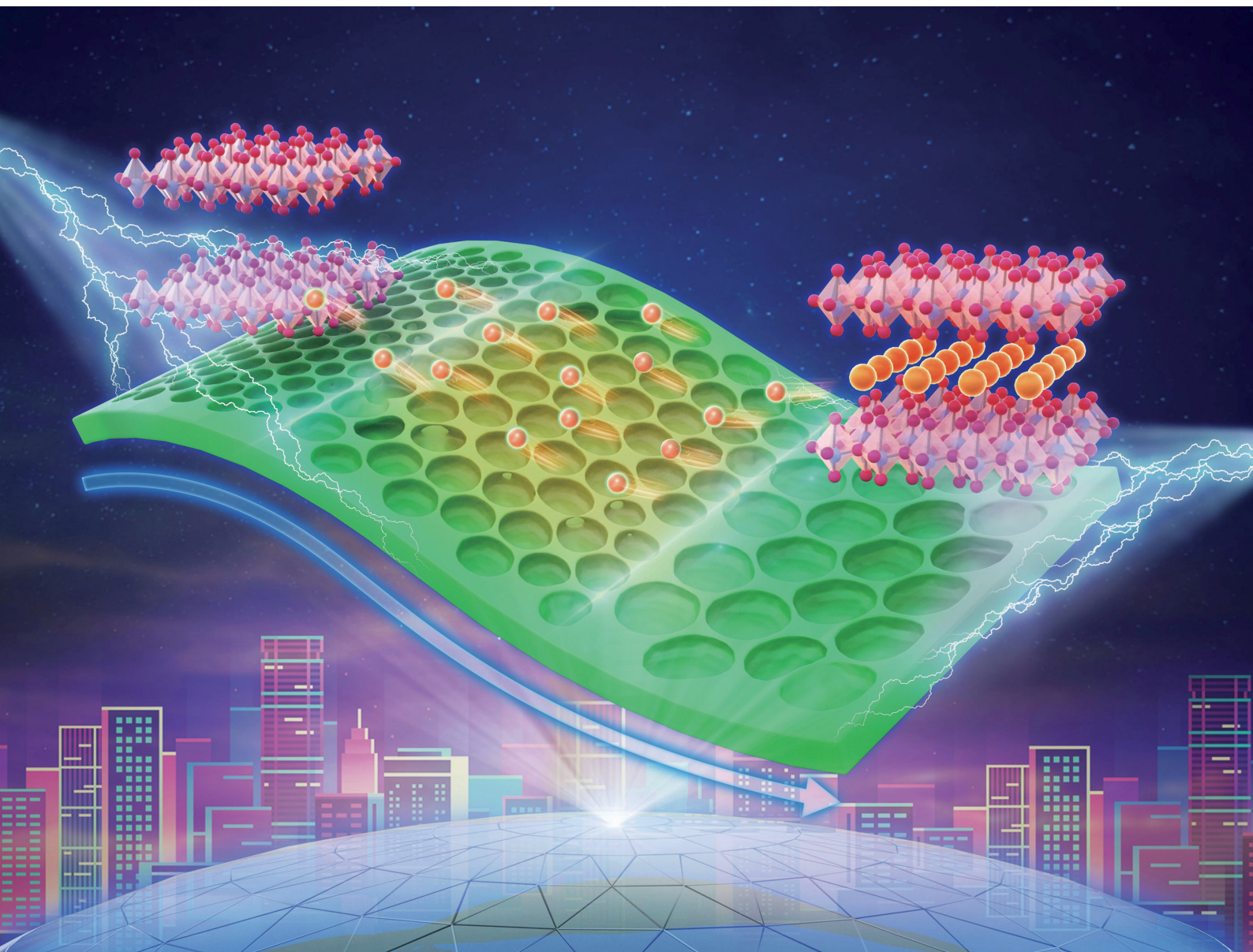


# Journal of Materials Chemistry C

Materials for optical, magnetic and electronic devices

[rsc.li/materials-c](https://rsc.li/materials-c)



ISSN 2050-7526


**PAPER**

Hua Li, Yahia Djaoued *et al.*  
2D vanadium oxide inverse opal films: cycling stability  
exploration as an electrochromic active electrode



Cite this: *J. Mater. Chem. C*, 2023, 11, 923

## 2D vanadium oxide inverse opal films: cycling stability exploration as an electrochromic active electrode†

Hua Li,<sup>\*ab</sup> Yuwei Liu,<sup>a</sup> Weihui Jiang,<sup>c</sup> Jian Liang,<sup>c</sup> Zijuan Tang,<sup>a</sup> Meilin Hu,<sup>a</sup> Jacques Robichaud<sup>b</sup> and Yahia Djaoued<sup>b</sup> <sup>\*b</sup>

2D vanadium oxide inverse opal (IO) films with a porous array were fabricated via a modified “dynamic hard template infiltration strategy” using various sizes of sacrificial polystyrene spheres (PS), followed by calcination under various conditions. Effects of pore size and phases on electrochromic cycling were explored by combining electrochemical cyclic voltammetry (CV) and chronoamperometry (CA). The results showed that the pore size has an important double influence on electrochromic cycling stability; on the one hand, pores buffered stress-induced pulverization for which the appropriate pore size under present conditions was found to be 141 nm. On the other hand, faster chemical dissolution in the film of a smaller pore size (V220-400C) led to accelerated fading in electrochromic cycling in contrast to its bigger pore size counterpart. In contrast, small amounts of  $V_6O_{13}$  and non-stoichiometric  $V_6O_{13+y}$  in the  $V_2O_5$  IO film were found to greatly improve cycling stability in both electrochemical CV and electrochromic cycles. This improved cycling stability was attributed to good conductivity of  $V_6O_{13+y}$  which greatly alleviated pulverization and chemical dissolution in  $V_2O_5$  IO films by minimizing the phase coexistence upon cycling. The correlation between electrochemical cycling stability and electrochromic cycling stability is also discussed.

Received 29th September 2022,  
Accepted 30th November 2022

DOI: 10.1039/d2tc04130h

rsc.li/materials-c

## Introduction

Vanadium oxides as electrochromic active materials are particularly attractive since they show polyelectrochromic behavior<sup>1,2</sup> as well as a fast response time<sup>3</sup> during the reversible intercalation/deintercalation of cations (such as  $Li^+$ ) into their typical layered structure due to the multiple stable oxidation states (III–V) of vanadium in its oxides. However, similar to their application in batteries, their practical use as electrochromic (EC) active materials was limited partially due to poor cycling reversibility and stability<sup>4</sup> that resulted in fast fading upon cycling. Unfortunately, the corresponding explorations of vanadium oxides as EC active electrode are scarce. Based on the

research on battery applications of vanadium oxides, their poor cycling reversibility was found to originate from stress-induced structural pulverization and chemical dissolution.<sup>5,6</sup> The insertion of Li-ions into the vanadium oxide electrode brings about a series of phase transformations (lithiation-induced phase transformations), which result in considerable heterogeneity accompanied simultaneously by the phase coexistence of the Li ions across the electrode architecture.<sup>7–9</sup> Such a heterogeneity leads to stress differentials between the discharged and charged states. It has been proved that this heterogeneity strongly depends on the particle dimensions and geometries, the nature of the interfaces and the relative positioning of the particles within the electrode architecture.<sup>10,11</sup> For example, Luo *et al.* have shown that, in contrast to its bulk counterpart, which showed an extended phase coexistence, nanosized  $V_2O_5$  undergoes consecutive transformations with minimal phase coexistence on discharge since it possesses higher porosity and thus faster Li-ion diffusion.<sup>12</sup> Therefore, the lattice-mismatched phase boundaries and the corresponding stress could be circumvented.

Except for achieving nanosized  $V_2O_5$ , the other way to minimize multiphase coexistence was to compositing it with a second phase<sup>13,14</sup> as an “elastic buffering phase” to release the stress. Furthermore, fabricating a hierarchical macro/micro/nano sized structure,<sup>15</sup> and/or introducing a pore structure<sup>16</sup> was also shown to alleviate stress. Alternatively, in order to increase

<sup>a</sup> Department of Materials Chemistry, School of Materials Science and Engineering, Jingdezhen Ceramic University, Jingdezhen, Jiangxi, 333403, P. R. China.  
E-mail: 201002@jci.edu.cn; Tel: +86 798 8499678

<sup>b</sup> Laboratoire de Recherche en Matériaux et Micro-spectroscopies Raman et FTIR, Université de Moncton-Campus de Shippagan, Shippagan, NB, E8S1P6, Canada.  
E-mail: Yahia.djaoued@umoncton.ca; Fax: +1 506 336 3437;  
Tel: +1 506 336 3400

<sup>c</sup> National Engineering Research Centre for Domestic & Building Ceramics, Jingdezhen Ceramic Institute, Jingdezhen, Jiangxi, 333001, P. R. China.  
Tel: +86 798 8499328

† Electronic supplementary information (ESI) available: Photographs of the electrolyte after cycling, CA and CV cycling, EIS, optical photographs of the films after cycling, and the SEM image. See DOI: <https://doi.org/10.1039/d2tc04130h>

conductivity and hence ion-diffusion, doping was also shown to possibly minimize phase coexistence, like doping with a high-valence cation, such as  $\text{Mo}^{6+}$  and  $\text{W}^{6+}$ ,<sup>17,18</sup> or even directly doping with conductive second phase, for instance carbon<sup>19</sup> or Ag.<sup>20</sup>

In addition to stress-induced structural pulverization, chemical dissolution is another key factor leading to fading during cycling. Since a series of vanadium-containing ions such as  $\text{H}_2\text{VO}_4^-$ ,  $\text{HVO}_4^{2-}$ ,  $\text{HV}_2\text{O}_5^-$ ,  $\text{VO}_2^+$ ,  $\text{VOH}^{2+}$  and  $\text{VO}^+$  are formed which are soluble in electrolyte,<sup>6,7</sup> various strategies were developed to suppress the chemical dissolution, like using a polymer gel electrolyte,<sup>21</sup> surface treatment of vanadium oxide films,<sup>22</sup> adding a second sacrificing phase, such as  $\text{V}_2\text{O}_3$ ,<sup>7</sup> and tuning the valence states of vanadium oxide composites.<sup>23,24</sup>

Although these above strategies significantly improved the electrochemical cycling stability for electrodes in batteries, the situation is different for EC devices (ECD) since transmittance of the vanadium oxide electrode during electrochromic cycling is always of primary importance in ECDs. Therefore, some of the above strategies are inapplicable in ECDs. First, doping with carbon is not possible since carbon materials strongly absorb in the whole light region. Second, the contact status between the vanadium oxide film and ITO substrates also importantly affects the optical contrast and EC cycling stability since the film could peel off from the substrate due to structural pulverization upon cycling. Third, different from most research in which cyclic voltammetry (CV) was used to characterize cycling stability of vanadium oxide as a battery electrode, its electrochromic behavior directly responds to chronoamperometry technology (CA), which requires a constant voltage. This could cause the intercalation of Li-ions to present different diffusion processes, leading to different structural changes or cycling properties. Therefore, recent strategies are mainly focusing on increasing the porosity. For instance, Li *et al.*<sup>25</sup> pioneered introducing inverse opal into a  $\text{V}_2\text{O}_5$  film, demonstrating its advantages for color modulation in the visible region, which they attributed to the higher surface area of the microporous structure. However, they did not report cycling stability results.

Apart from these strategies, although many reports have mentioned that pores in the electrode benefit cycling stability, it is unclear what role the pore size plays in that matter. In this work, we adapted our recently developed “dynamic hard template infiltration strategy”,<sup>26,27</sup> to fabricate a series of two-dimensional (2D)  $\text{V}_2\text{O}_5$  IO films of different pore sizes on ITO substrates, showing well arrayed pore structures, which were used to explore in depth the effect of the pore size and phase composition on cycling stability of vanadium oxides. This work also permitted understanding the correlation between electrochromic cycling stability and electrochemical cycling stability.

## Experimental

### Materials

The non-cross-linked monodispersed carboxyl polystyrene (PS) sphere aqueous suspensions (PS particles, 5.0% w/v) of

diameters 220, 430 and 700 nm, respectively, were purchased from SpheroTech Inc. Before use, they were diluted to 0.6% w/v with equal volumes of ethanol and water. Prior to use, the ITO coated glass substrates were ultrasonically treated for 15 min, successively in warm water, acetone, ethanol and deionized water.  $\text{NH}_4\text{VO}_3$ , analytically pure tetrahydrofuran (THF), sodium dodecylsulfate (SDS) and Millipore water was purchased from Sinoreagent Co. Ltd and used as received without further purification. All the aqueous solutions were prepared with Millipore water (resistance =  $18.2 \text{ M}\Omega \text{ cm}^{-1}$ ). The glass slides were immersed in a piranha solution (30%  $\text{H}_2\text{O}_2$ :concentrated  $\text{H}_2\text{SO}_4 = 3:7$ , v/v) at  $100^\circ\text{C}$  for 15 min, and then washed with Millipore water.

### Fabrication of the $\text{V}_2\text{O}_5$ monolayer inverse opal

2D  $\text{V}_2\text{O}_5$  monolayer inverse opal (IO) was synthesized using a “dynamic-hard template” infiltration strategy.<sup>26</sup> First, a clean functionalized glass slide was placed on the bottom of a Petri dish, followed by barely submerging the slide with Millipore water. The pure PS particle suspension (0.6% w/v) was added dropwise on the surface of the water over the glass slide to get a self-assembled monolayer of PS spheres on the water surface. Afterwards, a few drops of 2 wt% SDS solution were added into the water, which closely packed the PS monolayer, resulting in a 2D PS opal floating over the solution. Once the 2D self-assembly was achieved, the glass slide was gently removed. Then, water was removed, and 4 ml of water was left in the Petri dish while the PS opal was still floating on the water surface. The content of the Petri dish was then heated to  $50\text{--}60^\circ\text{C}$  and 20 ml of  $\text{NH}_4\text{VO}_3$  saturated aqueous solution ( $50^\circ\text{C}$ ) was added into the Petri dish. Then, a substrate was slid into the water underneath the 2D PS opal composite film, and the remaining solution was sucked out again of the Petri dish to make the floating film sink onto the substrate and form a 2D  $\text{NH}_4\text{VO}_3/\text{PS}$  opal composite film. A  $\text{V}_2\text{O}_5$  2D IO is obtained by annealing the  $\text{NH}_4\text{VO}_3/\text{PS}$  opal composite film at  $400^\circ\text{C}$  for 2 h under atmospheric conditions at a ramping speed of  $2^\circ\text{C min}^{-1}$ . According to the size of the PS template used, the obtained  $\text{V}_2\text{O}_5$  2D IO samples were named V220-400C, V430-400C, and V700-400C, respectively. Here, V represents vanadium oxide while the three succeeding digits refer to the diameter of the PS spheres in nm. The calcination temperatures were indicated by adding a dash symbol (“-”) followed by a calcination temperature in  $^\circ\text{C}$  plus a capital letter “C”. For instance, sample V220-400C is a  $\text{V}_2\text{O}_5$  2D IO templated from 220 nm PS spheres, calcined at  $400^\circ\text{C}$  under atmospheric conditions.

### Fabrication of mixed vanadium oxides monolayer inverse opal

A mixed vanadium oxide 2D IO templated from the 430 nm PS sphere sample (AV430-400C) was obtained by heat-treating the V430-400C sample under an argon atmosphere at  $400^\circ\text{C}$  for 0.5 h at a ramping speed of  $5^\circ\text{C min}^{-1}$ . Here, “A” in “AV430-400C” means that the V430-400C sample was treated under argon.

Another mixed vanadium oxides film (V430-310C) was attained by annealing the  $\text{NH}_4\text{VO}_3/\text{PS}$  opal composite film at



310 °C for 80 min under air atmosphere with a ramping speed of 3 °C min<sup>-1</sup>.

### Characterization

Cyclic voltammetry (CV) measurements were performed with a CHI600E electrochemical workstation (Chinstruments, Shanghai, China) using a three-electrode cell in the voltage range from -1 to 1 V at a 50 mV s<sup>-1</sup> cycling speed. The vanadium oxide thin films deposited on ITO substrates were used as working electrodes while a platinum grid served as a counter electrode and a commercial Ag/AgCl 1 M KCl electrode served as reference. A 0.5 mol L<sup>-1</sup> LiClO<sub>4</sub>/propylene carbonate solution was used as the electrolyte. The test parameters of electrochemical impedance spectroscopy (EIS) were set as follows: an AC voltage with 0.5 V and frequency range from 0.1 Hz to 10<sup>6</sup> Hz. The impedance spectrum consists of a semi-circle in the high frequency region and an inclined straight line in the low frequency region. The semi-arc represents the charge transfer resistance, and the straight line represents the diffusion of ions.<sup>28</sup> The data from the spectra were further fitted and analysed using ZView software, from which the charge transfer resistance could be directly obtained.

Electrochromic measurements were conducted by combining the optical transmittance spectra obtained using a UV-3600 spectrophotometer (Shimadzu, Tokyo, Japan) with the chronoamperometry technology (CA) using a CHI600E electrochemical workstation with an applied voltage from -1 to +1 V, in increasing potential steps of 180 s per step. The corresponding change in optical density ( $\Delta OD$ ) was defined as follows:

$$\Delta OD = \log(T_{\text{bleached}}/T_{\text{colored}}).$$

The coloration/bleaching switching behaviors of films on ITO glass were measured at a wavelength of 430 nm by alternately applying a square wave voltage of +1.0 V to -1.0 V for 40 s for

each state. The switching time is defined as the time required for reaching 90% of the film's full transmittance change.

SEM studies were performed using a S4800 FESEM system from Hitachi. Typically, the working distance was 3.2 mm and the accelerating voltage ranged from 1000 to 5000 V, with an emission current of 2300 to 5000 nA.

Micro-Raman spectra were recorded at room temperature using a Jobin-Yvon Labram HR microanalytical spectrometer. The spectra were generated with 17 mW, 632.8 nm, and He-Ne laser excitation and were dispersed with a 1800 grooves per mm grating across a length of 0.8 m of the spectrograph. Filters were used to vary the laser power as needed since low valence vanadium oxide is sensitive to laser heating. The spectral resolution is estimated to be less than 0.5 cm<sup>-1</sup> for a slit width of 150  $\mu$ m and a confocal hole of 300  $\mu$ m.

The optical transmittance spectra were monitored on a UV-3600 spectrophotometer (Shimadzu, Tokyo, Japan) in the wavelength range of 190–1100 nm.

## Results and discussion

### Effect of the pore size on cycling stability

Arrayed structural V<sub>2</sub>O<sub>5</sub> films of various pore sizes were successfully fabricated from template PS spheres of 220, 430 and 700 nm diameters. The nominal diameter (Fig. 1a–c) renders possible the investigation of the effect of the pore size on cycling stability of V<sub>2</sub>O<sub>5</sub> IO films regarding electrochemistry and electrochromism. Since the pore sizes of the IO films will not correspond to the nominal diameter of the PS spheres, we measured the actual pore size and wall and film thicknesses (Fig. 1e–g) of the samples using Nanomeasure software. The results are listed in Table 1. It was found that pore sizes increased from 141 nm for V220-400C to 254 nm for V430-400C and then greatly increased to 599 nm for V700-400C,

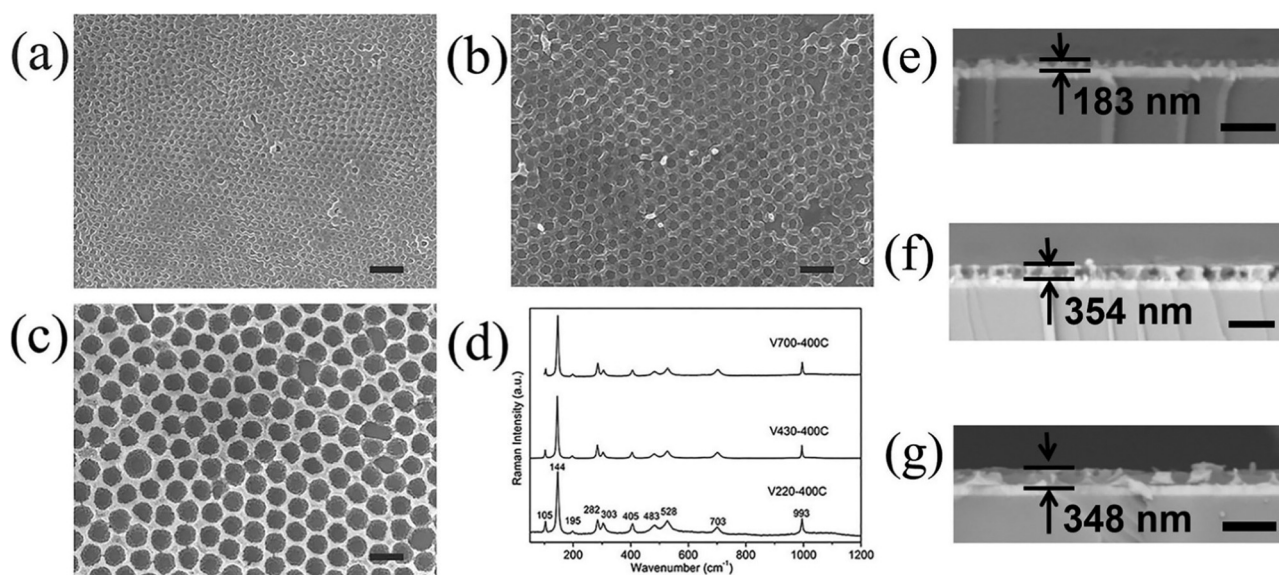


Fig. 1 SEM (a–c) and the corresponding cross-sectional images (e–g) and Raman spectra (d) of samples V220-400C (a and e), V430-400C (b and f) and V700-400C (c and g). Scale bar in a–g is 1  $\mu$ m.

Table 1 Pore structure parameters of V<sub>2</sub>O<sub>5</sub> IO films

Sample name	Pore size (nm)	Wall thickness (nm)	Film thickness (nm)	Ratio of pore size to wall thickness	Ratio of pore size to film thickness
V220-400C	141	98	183	1.44	0.77
V430-400C	254	172	354	1.47	0.72
V700-400C	599	158	348	3.79	1.72

respectively, while the wall thickness shows a drastic increase from 98 nm (V220-400C) to 172 nm (V430-400C) and then slightly decreases to 158 nm for V700-400C. This variation could be attributed to the difference of capillary action within the interstitial spaces of the PS sphere templates. Apart from the pore size and thickness of the walls, film thicknesses are also affected by the size of the PS templates: 183 nm for V220-400C, 354 nm for V430-400C and 348 nm for V700-400C, respectively.

Fig. 1d shows the Raman spectra of V220-400C, V430-400C and V700-400C samples. Characteristic Raman modes of  $\alpha$ -V<sub>2</sub>O<sub>5</sub> emerged at  $\sim$ 105, 144, 195, 282, 303, 405, 483, 528, 703, and 993 cm<sup>-1</sup>. The low frequency modes at  $\sim$ 105, 144, and 195 correspond to the relative motions of V<sub>2</sub>O<sub>5</sub> layers (external modes).<sup>26</sup> The two peaks at 144 and 195 cm<sup>-1</sup> were strongly associated with the layered structure, demonstrating its long-range structural order.<sup>27</sup> The intermediate frequency peaks at  $\sim$ 282, 303, 405, 483, 528, and 703 cm<sup>-1</sup> are attributed to the bending and stretching vibrations (internal modes) of the V–O bond in V<sub>2</sub>O<sub>5</sub>.<sup>30</sup> The highest frequency peak at  $\sim$ 993 cm<sup>-1</sup> corresponds to the stretching mode of the terminal oxygen (vanadyl oxygen, V=O<sub>v</sub>). In accordance with the literature,<sup>27–30</sup> the absence of a mode at 840 cm<sup>-1</sup>, which is Raman active in defective V<sub>2</sub>O<sub>5</sub>, confirmed good crystallinity of the  $\alpha$ -V<sub>2</sub>O<sub>5</sub> phase within the film.

Fig. S1 (ESI†) shows the impedance spectra of V220-400C, V430-400C and V700-400C samples. V220-400C has a close charge transfer resistance of 95.48  $\Omega$  to that of V430-400C (96.43  $\Omega$ ) and a similar ion diffusion since the semicircle at the high frequency and the straight line in the low frequency region almost overlap. Oppositely, a smaller charge transfer resistance of 73.68  $\Omega$  and slower diffusion of ions were evidenced in V700-400C since it shows a narrower semicircle diameter and a less steep straight line. The values are well consistent with their corresponding ratio of the pore size to film thickness or ratio of the pore size to wall thickness (Table 1); V220-400C and V430-400C have close values of the ratio of pore size to film thickness but much smaller than that of V700-400C. The above results indicate that, regarding ion diffusion, appropriate pore size is important.

The electrochemical cycling performance of V220-400C, V430-400C and V700-400C samples was investigated by cycling voltammetry (CV) (Fig. 2). Similar to that found in the literature,<sup>3,27</sup> the anodic oxidation peaks, which were measured at the 10th cycle, for all three samples are close for the first peak, being around  $-0.6$  V for V220-400C,  $-0.58$  V for V430-400C and  $-0.59$  V for V700-400C, indicating a similar behavior of Li<sup>+</sup> deintercalation. As the voltage increased, we observe

another anodic peak at  $+0.76$  V for V220-400C,  $+0.85$  V for V430-400C and  $+0.69$  V for V700-400C. Also, the cathodic reduction peak for V700-400C is around  $-0.23$  V, higher than those of V430-400C ( $-0.37$  V) and V220-400C ( $-0.29$  V), which could be attributed to its lower charge transfer resistance.

Although capacity fading occurred for all three samples during CV cycling, their fading behavior was different (Fig. 2(a)–(c)). A fast fading was observed in V220-400C for the first 50 cycles while there was no obvious fading after 100 cycles. In contrast, V430-400C showed a relatively gentle change during the whole 200 cycles. On the other hand, for V700-400C, there was a fast fading in the first 50 cycles like V220-400C, followed by a gentle fading for the remaining cycles. The optical photos before and after 200 cycles are shown in Fig. 2d (V220-400C), 2e (V430-400C) and 2f (V700-400C). In Fig. 2d after 200 cycles, it is observed that the bottom image is less vibrant than the top one but still shows a uniform film indicating that, in contrast to its counterparts with bigger pore sizes (V430-400C, V700-400C), V220-400C remained well attached onto the ITO substrate and that its capacity fading was likely due to chemical dissolution.

Differently, in addition to chemical dissolution, partial peeling off of the film from the substrate was also observed in both V430-400C and V700-400C, which indicated that structural breakdown occurred during cycling. As shown in Table 1, the film thickness of V430-400C (354 nm) is close to that of V700-400C (348 nm) and nearly double that of V220-400C (183 nm); nonetheless, V430-400C and V220-400C have close charge transfer resistances of 95.48  $\Omega$  and 96.43  $\Omega$ , respectively, and a similar diffusion of ions. As we discussed before, the film thickness is close to the pore depth. A higher pore depth indicates a bigger strain difference between the bottom and top of the film since the bottom is attached onto the ITO substrate. In our experiment, the pore depth depends on the size of the PS spheres and the capillary action between them. Therefore, it could be reasonably deduced that the pore size plays an important role in structural pulverization and peeling off. Once the film thickness is reduced enough to undermine the effects from the bottom, capacity fading is mostly due to chemical dissolution. Hence, moderate capacity fading in V430-400C and V220-400C in comparison to that of V700-400C corresponds to the much lower ratio of the pore size to film thickness (0.77 for V220-400C, 0.83 for V430-400C and 1.72 for V700-400C). In the present experiment, we note that, to get an appreciable effect, the pore size should be smaller than 254 nm.

Based on the results of electrochemical CV cycling, V220-400C and V430-400C were chosen to compare electrochromic cycling performance (Fig. 3) through chronoamperometry (CA).

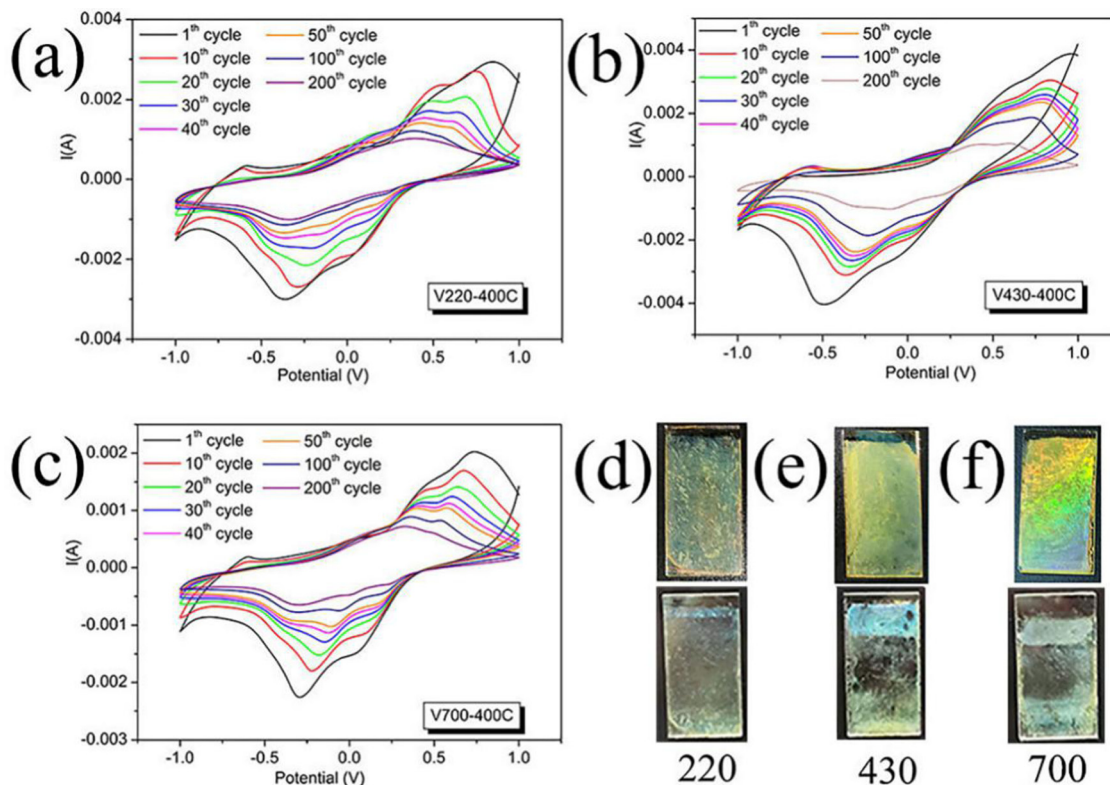


Fig. 2 Room temperature cyclic voltammograms and the corresponding optical photos before (top photos in d–f) and after 200 cycles (bottom photos in d–f) at a potential window of  $\pm 1.0$  V in  $0.5 \text{ mol L}^{-1}$  LiClO<sub>4</sub>/propylene carbonate solution at a sweep rate of  $50 \text{ mV s}^{-1}$  for samples V220-400C (a and d), V430-400C (b and e) and V700-400C (c and f).

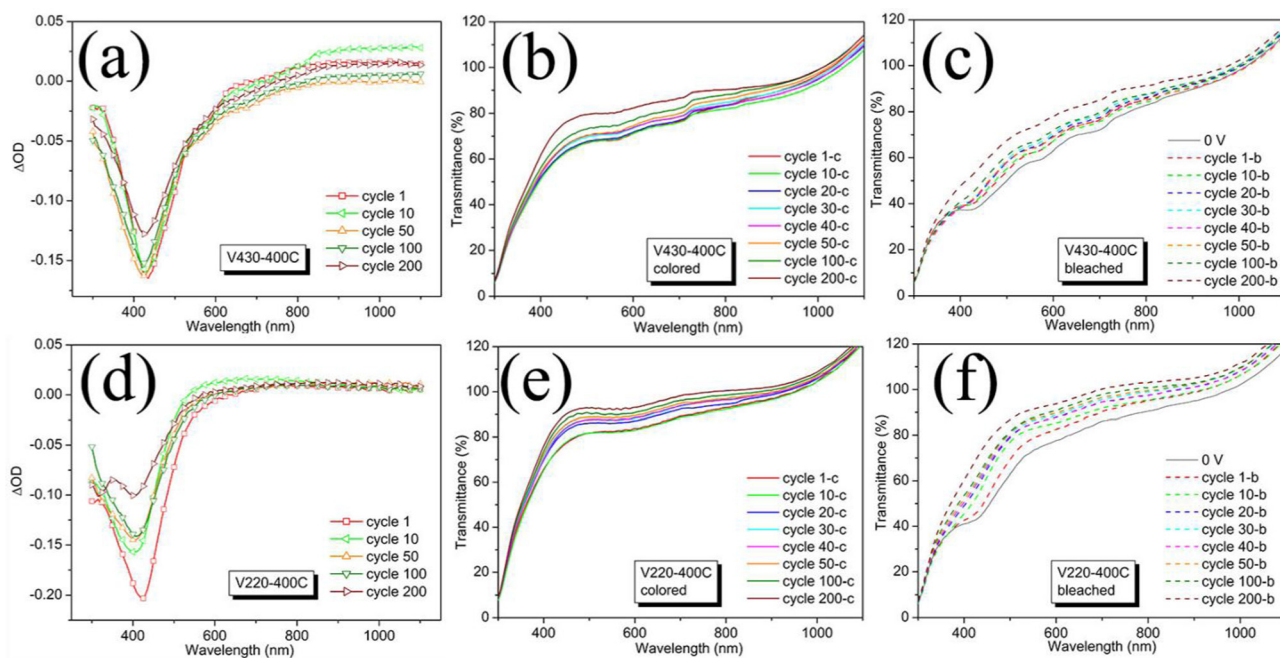


Fig. 3 Optical density and the corresponding transmittance in the colored state at  $-1.0$  V and bleached state at  $+1.0$  V for samples V430-400C (a–c) and V220-400C (d–f) during cycling.

During coloration/bleaching under an applied voltage of  $\pm 1.0$  V, both samples showed increasingly changing transmittance in the near-ultraviolet region, especially at a wavelength of around 420 nm, where the largest change in optical contrast is found as the



number of cycles increases, while in the near-infrared region, the transmittance change is less (Fig. 3a and d).

This indicated that both samples have a double electrochromic effect, *i.e.*, an anodic electrochromic effect in the near ultraviolet region and a cathodic effect in the near infrared region.<sup>31,32</sup> Considering the low  $\Delta OD$  in the near-infrared region (700 nm to 1100 nm) under present conditions, we will restrict our discussion to the region ranging from near-ultraviolet to visible (300 to 600 nm). Apart from this, both samples showed a gradual increase in transmittance both in colored and bleached states during electrochromic cycling (Fig. 3b, c and e, f). An obvious dissolution was found both in V430-400C and V220-400C; after 200 cycles the electrolyte solution became yellowish compared to its original colorless aspect (ESI†, Fig. S2) except that V430-400C shows superior dissolution since its electrolyte has a darker yellowish color.

The response times (coloring ( $t_c$ ) and bleaching ( $t_b$ )) were studied to understand the effect of electrochemical resistance on electrochromic properties. Response time is defined as the time required for the coloring and bleaching process to achieve 90% of the total optical modulation of the electrochromic device (ECD).<sup>33</sup> The time-dependent transmittance curves at a wavelength of 430 nm are taken *in situ* while the CA measurements are performed. The response times of the ECDs during cycling are shown in Fig. S3 (ESI†). Samples V220-400C and V430-400C show close coloring times of 26.56 and 24.82 s, respectively; while V220-400C shows a much shorter bleaching time of 4.03 s as compared to 27.13 s for V430-400C.

Different from the CV observation, in which a gradual fading occurred in V430-400C (Fig. 2b), we found a relatively stable but slightly decreased  $|\Delta OD|$  before 100 cycles followed by a larger change from the 100th cycle to the 200th cycle (Fig. 3a). Combining the corresponding CA results (Fig. S4a and c, ESI†), a stable current until the 100th cycle and then a gradual reduction beginning at the 130th cycle is observed, which confirmed the large change in  $\Delta OD$  from the 100th cycle to the 200th cycle. This observation is consistent with the optical photographs by comparing the one at 100 cycles to the one at 200 cycles; after 100 cycles, a bluish homogeneous film is seen while after 200 cycles, the middle part of the film had disappeared, revealing the substrate, indicating that its ordered structure had collapsed (Fig. S4b and d, ESI†). Therefore, it could be deduced that upon cycling, both dissolution and stress-induced structural collapse co-contributed to the fading of the electrochromic optical density. Furthermore, dissolution accompanied the whole electrochromic process, leading to a gradual reduction of optical density.

The  $\Delta OD$  for V220-400C shows a drastic change from the beginning of cycling: a much higher  $|\Delta OD|$  at the first cycle than for the following cycles, indicating a strong reduction of Li-ion intercalation after the 1st cycle. The corresponding CA validated this observation: the current quickly reduced right after the first cycle (Fig. S5a, ESI†). Interestingly, the fast fading in the primary 50 cycles was also observed in CV though there was no vigorous change in the first 10 cycles (Fig. 2a). This is probably because of the difference in the Li-ion intercalation

process, where a constant voltage of 1.0 V is applied in CA as compared to a gentle increase in the applied voltage from  $-1.0$  to 1.0 V in CV. This smooth change of the applied voltage in CV minimizes the speed heterogeneity of Li-ion intercalation. Therefore, in CV several soluble vanadium compounds having different valences of V-ions were formed under a limited speed, which led to gradual capacity fading. In contrast, in the CA electrochromic process, the prompt application of voltage as high as 1.0 V led to the simultaneous formation of various soluble vanadium compounds with a mixed valence of V-ions from the beginning, as a result of which, fast dissolution was found in the first cycle and fast fading in the optical density right after the 1st cycle. The following cycles in both CA and CV showed relatively stable values until the 100th cycle. Although there was no obvious change in CA from the 100th to 200th cycle, a large capacity fading at around 420 nm wavelength was observed. In contrast to V430-400C in which half of the film was destroyed after 200 cycles, the V220-400C film is almost intact with negligible damage as shown in Fig. S3c (ESI†). Considering the above results from V220-400C and V430-400C, it is reasonable to deduce that a pore size as small as 141 nm for V220-400C could effectively “buffer” stress-induced structural pulverization but that chemical dissolution is governed by the chemical stability of the oxides, unrelated to pore size. Therefore, as compared with V430-400C, in V220-400C, which has a higher surface area and a thinner porous framework, a faster intercalation of Li-ion and accordingly a faster formation of soluble vanadium compound could be expected, which resulted in a faster fading during electrochromic cycling.

Apart from this, we found an increased  $\Delta OD$  at a wavelength of 430 nm as the pore size decreased for the first cycle; the  $\Delta OD$  of V220-400C is 0.21, higher than that of V430-400C (0.17), which is higher than for most planar films ( $\Delta OD < 0.15$ , Table S1, ESI†).<sup>34–36</sup> However, our  $\Delta OD$  values are smaller than those (0.33 and 0.28) reported in the literature for 3D ordered macroporous  $V_2O_5$  films (3DOM) (Table S1 and ref. S1, ESI†).<sup>37</sup> Considering the much higher thickness of these 3DOM (1100 nm), as compared to the present film (pore size 141 nm, thickness 183 nm), the lower  $\Delta OD$  of V220-400C could be attributed to lesser amount of  $V_2O_5$  in the film. After 100 cycles, the  $\Delta OD$  of V220-400C decreased to 0.16 as an effect from the chemical dissolution.

### Effect of phases on cycling stability

As discussed above, chemical dissolution is unavoidable if we chose a single  $V_2O_5$  phase. During electrochemical cycling, vanadium ions kept on changing their valences and accordingly the type of lithium vanadates during Li ion intercalation/deintercalation. This valence change is closely related to conductivity; when conductivity is low, there is necessarily a high polarization, which reduces the Li ion diffusivity.<sup>12,38</sup> On one hand this results in coexistence of multiphases of lithium vanadates and heterogeneity deterioration in the film, leading to a heterogeneous phase change and stress-induced pulverization. On the other hand, the coexistence of multiphases increased the possibility of simultaneous appearance of various

soluble vanadium compounds, which accelerated chemical dissolution. Therefore, the improvement of conductivity could be a way to reduce chemical dissolution.

Based on the above analysis, the best way to improve conductivity without sacrificing electrochromic optical contrast would be to directly increase conductivity by doping<sup>4,7</sup> or introducing a second conductive phase which has a low absorption in the visible region and be active to lithiation.

As a mixed-valence vanadium oxide,  $V_6O_{13}$  shows a combination of metallic character<sup>39</sup> at room temperature and high electrochemical capacity.<sup>40</sup> Here, we attempted to introduce a second conductive phase by simply heat-treating the obtained V430-400C, which is an  $\alpha$ - $V_2O_5$  phase, under an argon atmosphere at 400 °C for 0.5 h at a ramping speed of 5 °C min<sup>-1</sup>. As mentioned in the experimental section the obtained sample was named AV430-400C. Also, another mixed vanadium oxide film (V430-310C) was obtained by annealing the  $NH_4VO_3$ /PS opal composite film at 310 °C for 80 min at a ramping speed of 3 °C min<sup>-1</sup> under atmospheric conditions.

Fig. 4a shows the Raman spectra of AV430-400C and V430-310C samples. In both spectra, the peaks indicated in red located at 166, 844, 880, 935, 992, 996 and 1033 cm<sup>-1</sup> are attributed to the mixed-valence phase  $V_6O_{13}$ .<sup>41</sup> The peaks at 105, 144, 282, 303, 405, 483, 528, 703 and 993 cm<sup>-1</sup> are attributed to  $\alpha$ - $V_2O_5$ .<sup>29,40</sup> Unidentified peaks appearing at 910, 946 and 1009 cm<sup>-1</sup> (indicated in blue) could be attributed to the non-stoichiometric phases between  $V_6O_{13}$  and  $\alpha$ - $V_2O_5$ .<sup>40</sup>

Both AV430-400C and V430-310C are composed of a mixed phase of  $V_6O_{13}$  and  $\alpha$ - $V_2O_5$  but with different ratios. AV430-400C is mainly composed of  $\alpha$ - $V_2O_5$  but with a little amount of  $V_6O_{13}$  as a second phase while for V430-310C, it is the opposite. Both of them show a close charge transfer resistance (55.14  $\Omega$  for AV430-400C, 59.68  $\Omega$  for V430-310C) but different ion diffusion. AV430-400C has a faster ion diffusion with a steeper slope in the low frequency region than V430-310C (Fig. S6, ESI†). There is a dramatic difference in the CV results between V430-310C and AV430-400C. The anodic peak for AV430-400C was positively moved to -0.19 V in comparison to -0.58 V for V430-400C while the cathodic peak negatively moved to -0.67 V from -0.37 V in V430-400C. On the other hand, the anodic peak for V430-310C was around 0.3 V while the cathodic peak was around -0.36 V. The difference between AV430-400C and V430-310C could be attributed to the phase composition difference.

Similar to reports on  $V_6O_{13}$ ,<sup>41,42</sup> V430-310C showed a fast fading in the first 10 cycles batch (Fig. 4b) with attenuated fading capacity in the following cycles batches;  $V_6O_{13}$  undergoes four phase transitions from  $Li_{0.67}V_6O_{13}$  to  $LiV_6O_{13}$ ,  $Li_2V_6O_{13}$ , and  $Li_3V_6O_{13}$ , in sequence and decrease of electronic conductivity upon lithium insertion,<sup>43,44</sup> which accordingly increases the possibility of polarization and chemical dissolution. In particular, the slower ion diffusion deteriorated the coexistence of four phases and the corresponding polarization upon cycling, since the film partially peeled off from the

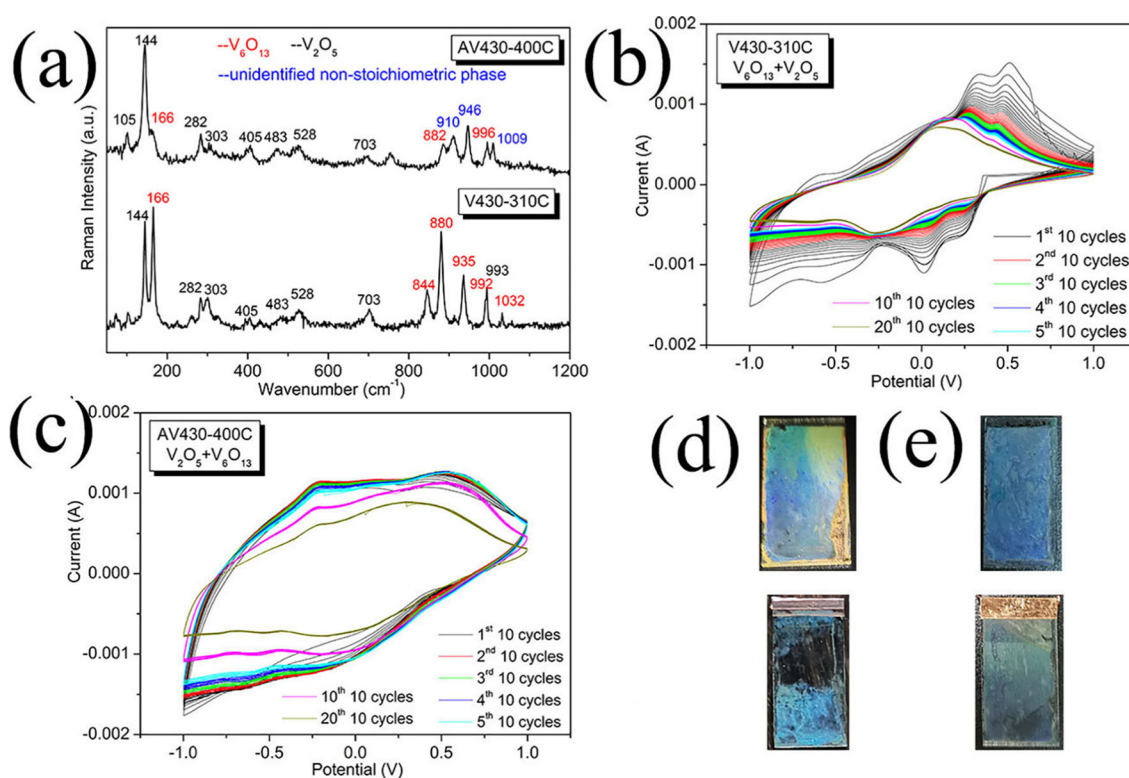


Fig. 4 Raman spectra (a), room temperature cycling voltammograms (b and c) and the corresponding optical photos before (up photos d and e) and after (bottom photos d and e) cycling conducted for samples V430-310C (b and d) and AV430-400C (c and e) at a potential window of  $\pm 1.0$  V in 0.5 mol L<sup>-1</sup> LiClO<sub>4</sub>/propylene carbonate solution at a sweep rate of 50 mV s<sup>-1</sup>.



substrate after 200 cycles (Fig. 4d, bottom). As a result, stress-induced pulverization occurred in V430-310C after cycling.

Aided by the presence of a small amount of  $V_6O_{13}$  in AV430-400C, its conductivity is greatly increased since its charge transfer resistance ( $55.14\ \Omega$ ) is smaller than that of V430-400C ( $96.43\ \Omega$ ). This accelerated the reaction kinetics and minimized polarization during cycling due to the coexistence of multiphases and consequently increased its capacity by showing a kind of pseudo-capacitive behavior.<sup>45</sup> Furthermore, in a porous structure, the reaggregation of the nano sized particles into large-size grains could be effectively avoided. As a result, the cycling stability was highly improved.

A much higher capacity is found for AV430-400C (Fig. 4c) than for V430-400C, although its pore size (260 nm) and film thickness (334 nm) (Fig. S7, ESI†) are close to those of V430-400C (pore size = 254 nm, film thickness = 354 nm). This could be partially attributed to the contribution from non-stoichiometry vanadium oxide in the film. Indeed, Murphy's group noted that non-stoichiometric  $V_6O_{13+y}$  showed a larger capacity than its stoichiometric analog  $V_6O_{13}$ .<sup>46</sup>

Assisted by a small amount of  $V_6O_{13}$ , AV430-400C remained intact after 200 cycles (Fig. 4e, bottom). Furthermore, except for the first 10-cycles which shows a gentle fading, an excellent cycling stability with a good reversible capacity was found in the first 50 cycles due to improved conductivity from  $V_6O_{13}$ , which reduced polarization and minimized multiphase coexistence during  $\alpha$ - $V_2O_5$  CV cycling. After 50 cycles, a small fading is observed from the 50th to the 200th cycle.

Based on the CV results, AV430-400C was further used to explore its electrochromic cycling stability. For ECD AV430-400C, the coloring and bleaching times were measured to be 19.9 s and 20.77 s, respectively, faster than for V430-400C (24.82 s for coloring and 27.13 s for bleaching), indicating the positive role from its low charge transfer resistance ( $55.14\ \Omega$  for V430-400C and  $96.43\ \Omega$  for V430-400C).

Assisted by a little amount of  $V_6O_{13}$ , AV430-400C showed a relatively higher optical contrast (Fig. 5a) not only in the visible but also in the near-infrared (600–850 nm) regions for the first 50 cycles in contrast to its counterpart V430-400C. However, for the following cycles, the  $\Delta OD$  in the near-infrared region (600–850 nm) is close to 0, indicating a somewhat similar behavior to V430-400C which is a single  $\alpha$ - $V_2O_5$  phase. Also, there is an initially smaller absolute value of  $\Delta OD$  ( $|\Delta OD|$ ) in the visible region, taking 380 nm wavelength as an example,  $|\Delta OD| = 0.11$  for the 1st cycle followed by a gradual increase for the following 50 cycles to  $|\Delta OD| = 0.17$  for the 50th cycle. In the near-infrared region,  $|\Delta OD|$  gradually decreases with the number of cycles.

These results explain the change in electrochromic  $\Delta OD$  occurring from the 10th to 50th cycle. A slow fading cycling occurring from the 41st to the 199th cycle with a knee around cycle 80 indicates fading in  $\Delta OD$  with a noticeable change between the 50th and 100th cycle. After the 100th cycle, a stable CA revealed a stable  $\Delta OD$ . After 200 cycles, the film was nearly intact with a little pulverization on top (Fig. S8e, ESI†). According to the Raman spectrum of AV430-400C after 200 cycles

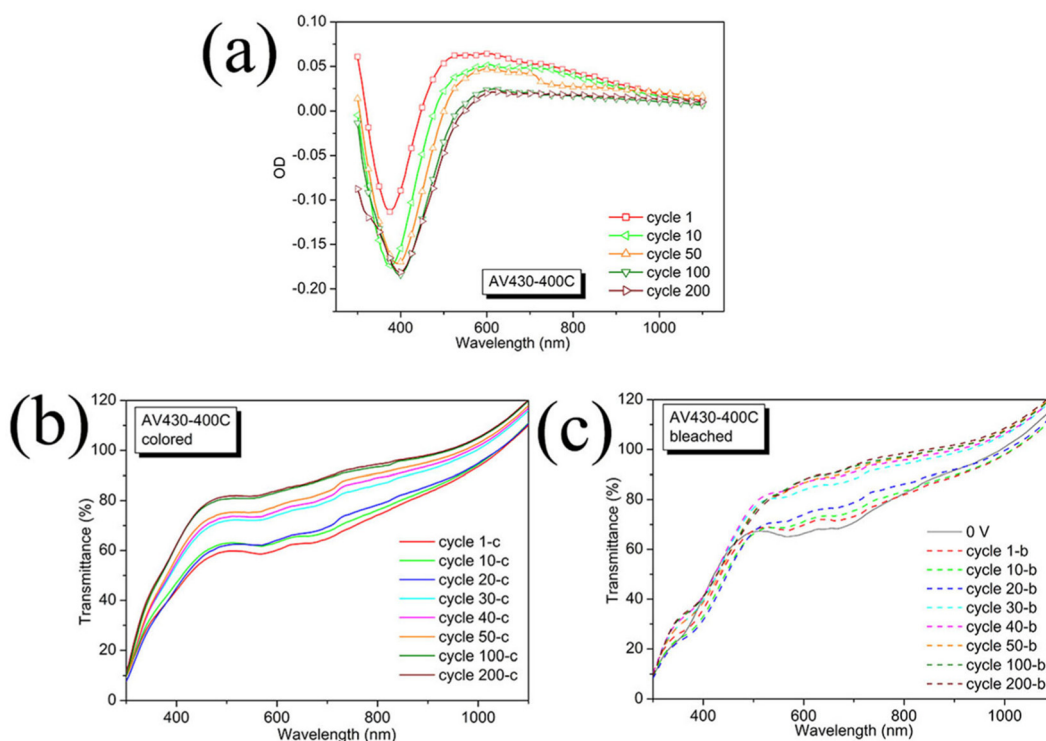


Fig. 5 Change in optical density (a) for sample AV430-400C and the corresponding transmittance under applied voltages of  $-1.0\ V$  (b) and  $+1.0\ V$  (c) for 180 s, respectively.

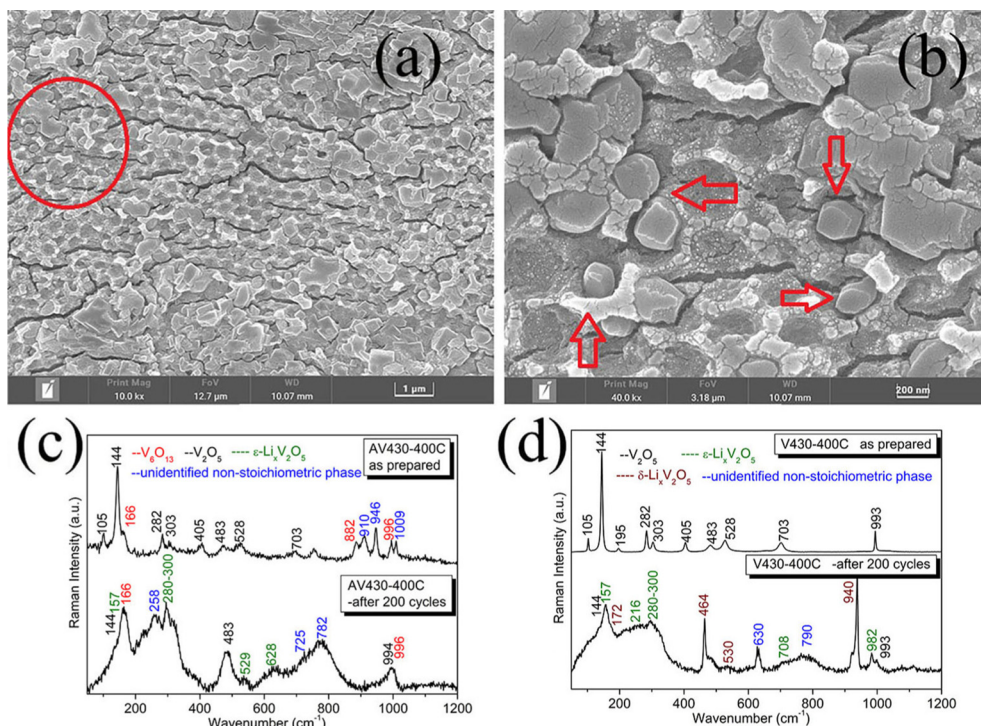


Fig. 6 (a) SEM images of sample AV430-400C cycled 200 times, (b) an HRSEM image of the encircled portion in SEM image (a). (c) Raman spectra of sample AV430-400C before cycling (top spectrum) and after 200 cycles (bottom spectrum). (d) Raman spectra of V430-400C before cycling (top spectrum) and after 200 cycles (bottom spectrum). SEM scale bars are 1  $\mu\text{m}$  in (a) and 200 nm in (b).

(Fig. 6c, bottom), the  $\alpha\text{-V}_2\text{O}_5$  phase almost disappeared with the  $\text{V}_6\text{O}_{13}$  phase remaining, confirming the dissolution of the  $\alpha\text{-V}_2\text{O}_5$  phase during cycling. Besides several unidentified Raman modes, the characteristic peaks of  $\epsilon\text{-Li}_x\text{V}_2\text{O}_5$  are also seen at around 157, 280–300, 529 and 628  $\text{cm}^{-1}$ .<sup>47–49</sup> In accordance with the Raman results, the corresponding SEM images (Fig. 6a and b) of AV430-400C after 200 cycles, show that the wall in the framework is almost collapsed, and furthermore, some column-like crystallites were formed within the pores of the IO film as highlighted by arrows (Fig. 6b). It could be deduced that after 200 cycles, some irreversible phases are formed, including  $\epsilon\text{-Li}_x\text{V}_2\text{O}_5$ .

Nonetheless, a better reversibility is obvious for AV430-400C in comparison to V430-400C; for V430-400C (Fig. 6d), the  $\alpha\text{-V}_2\text{O}_5$  phase has almost disappeared totally after cycling, which was replaced by  $\epsilon\text{-Li}_x\text{V}_2\text{O}_5$  with peaks at 157, 216, 280–300, 708 and 982  $\text{cm}^{-1}$  and the  $\delta\text{-Li}_x\text{V}_2\text{O}_5$  phase<sup>50</sup> with peaks at 172, 464, 530, and 940  $\text{cm}^{-1}$ , indicating that Li-ions were deeply and irreversibly entrapped within the film. In contrast, for AV430-400C, good conductivity rendered better reversibility during cycling which greatly minimized the phase co-existence and dissolution of  $\text{V}_2\text{O}_5$  and therefore rendered better electrochromic cycling stability.

Similar to some  $\text{V}_2\text{O}_5$  films mixed with a second phase (Table S1, ESI<sup>†</sup>),<sup>51,52</sup> the stability was greatly improved since  $\Delta\text{OD}$  at a wavelength of 430 nm for AV430-400C increased from 0.175 for cycle 10 to 0.18 for cycle 100 and retained this value until cycle 200 as compared with the pure  $\text{V}_2\text{O}_5$  film of the V430-400C sample, whose  $\Delta\text{OD}$  dropped from 0.16 in

cycle 10 to 0.15 in cycle 100 and then dramatically to 0.13 in cycle 200.

All things considered, both electrochromic and electrochemical cycling stabilities could be greatly improved simply by introducing a small amount of  $\text{V}_6\text{O}_{13}$  and non-stoichiometric  $\text{V}_6\text{O}_{13+y}$  into the  $\text{V}_2\text{O}_5$  film due to its high conductivity and large capacity.

## Conclusions

By comparing 2D  $\text{V}_2\text{O}_5$  IO monolayer films of various pore sizes, we demonstrated that  $\text{V}_2\text{O}_5$  films with an appropriate small pore of 140 nm (V220-400C) could effectively ‘buffer’ stress-induced pulverization in contrast to their analogs V430-400C and V700-400C having bigger pore sizes. Despite good resistance to pulverization, chemical dissolution was still unavoidable due to the inherent chemical instability of  $\text{V}_2\text{O}_5$  during electrochemical cycling.

With the addition of a little non-stoichiometric  $\text{V}_6\text{O}_{13+y}$ , cycling stability of AV430-400C, in both electrochromism and electrochemistry, was greatly improved in comparison to that of its  $\text{V}_2\text{O}_5$  counterpart V430-400C. The excellent cycling stability could be attributed to the better conductivity which reduced multiphase coexistence upon cycling. Therefore, on one hand, the quick dissolution of various vanadium compounds during intercalation/deintercalation of Li-ions was well minimized. On the other hand, stress-induced pulverization was

simultaneously alleviated due to minimized polarization under higher conductivity.

## Author contributions

Hua Li: conceptualization, data curation, investigation, methodology, funding acquisition, project administration and writing – original draft. Yuwei Liu: data curation, investigation, and methodology. Jian Liang: conceptualization, data curation and investigation. Weihui Jiang: funding acquisition and resources. Meilin Hu: validation. Zijuan Tang: investigation and validation. Jacques Robichaud: data curation, formal analysis, and writing – review & editing. Yahia Djaoued: data curation, funding acquisition, methodology, resources, project administration, and writing – review & editing.

## Conflicts of interest

There are no conflicts to declare.

## Acknowledgements

The financial support from the National Sciences and Engineering Research Council (NSERC) of Canada (grant #2017-05094), the John R. Evans Leaders Fund (Canada Foundation for Innovation) (grant #27741), the Research Assistantships Initiative of New Brunswick Innovation Fund (NBIF), Education Commission of Jiangxi Province of China (GJJ201317), and Jingdezhen Science and Technology Development Funds (20202GYZD013-11) is gratefully acknowledged.

## References

- G. Salek, B. Bellanger, I. Mjejri, M. Gaudon and A. Rougier, Polyol Synthesis of Ti-V<sub>2</sub>O<sub>5</sub> Nanoparticles and Their Use as Electrochromic Films, *Inorg. Chem.*, 2016, **55**, 9838–9847.
- S. Zanarini, F. Di Lupo, A. Bedini, S. Vankova, N. Garino, C. Francia and S. Bodoardo, Three-colored electrochromic lithiated vanadium oxides: the role of surface superoxides in the electro-generation of the red state, *J. Mater. Chem. C*, 2014, **2**, 8854–8857.
- H. Liu, X. Liang, T. Jiang, Y. Zhang, S. Liu, X. Wang, X. Fan, X. Huai, Y. Fu, Z. Geng and D. Zhang, Analysis of structural morphological changes from 3DOM V<sub>2</sub>O<sub>5</sub> film to V<sub>2</sub>O<sub>5</sub> nanorods film and its application in electrochromic device, *Sol. Energy Mater. Sol. Cells*, 2022, **238**, 111627.
- Y. Lu, L. Liu, D. Mandler and P. S. Lee, High switching speed and coloration efficiency of titanium-doped vanadium oxide thin film electrochromic devices, *J. Mater. Chem. C*, 2013, **1**, 7380–7386.
- H.-S. Wu, G. Zhou, L.-C. Yin, W. Ren, F. Li and H.-M. Cheng, Graphene/metal oxide composite electrode materials for energy storage, *Nano Energy*, 2012, **1**, 107–131.
- M. Yu, Y. Zeng, Y. Han, X. Cheng, W. Zhao, C. Liang, Y. Tong, H. Tang and X. Lu, Valence-Optimized Vanadium Oxide Supercapacitor Electrodes Exhibit Ultrahigh Capacitance and Super-Long Cyclic Durability of 100000 Cycles, *Adv. Funct. Mater.*, 2015, **25**, 3534–3540.
- Y. Song, T.-Y. Liu, B. Yao, T.-Y. Kou, D.-Y. Feng, X.-X. Liu and Y. Li, Amorphous mixed-valence vanadium oxide/exfoliated carbon cloth structure shows a record high cycling stability, *Small*, 2017, **13**, 1700067.
- Y.-S. Yu, M. Farmand, C. Kim, Y. Liu, C. P. Grey, F. C. Strobridge, T. Tylliszczak, R. Celestre, P. Denes, J. Joseph, H. Krishnan, F. R. N. C. Maia, A. L. D. Kilcoyne, S. Marchesini, T. P. C. Leite, T. Warwick, H. Padmore, J. Cabana and D. A. Shapiro, Three-dimensional localization of nanoscale battery reactions using soft X-ray tomography, *Nat. Commun.*, 2018, **9**, 921.
- L. R. De Jesus, J. L. Andrews, A. Parija and S. Banerjee, Defining diffusion pathways in intercalation cathode materials: some lessons from V<sub>2</sub>O<sub>5</sub> on directing cation traffic, *ACS Energy Lett.*, 2018, **3**, 915–931.
- C. Siu, M. J. Zuba, Y. Zong, H. Zhou, N. A. Chernova, L. F. J. Piper, G. Zhou and M. Stanley, Whittingham, Enhanced high-rate performance of nanosized single crystal ε-VOPO<sub>4</sub> with niobium substitution for lithium-ion batteries, *J. Electrochem. Soc.*, 2021, **168**, 060519.
- H.-G. Steinrück, C. J. Takacs, H.-K. Kim, D. G. Mackanic, B. Holladay, C. Cao, S. Narayanan, E. M. Dufresne, Y. Chushkin, B. Ruta, F. Zontone, J. Will, O. Borodin, S. K. Sinha, V. Srinivasan and M. F. Toney, Concentration and velocity profiles in a polymeric lithium-ion battery electrolyte, *Energy Environ. Sci.*, 2020, **13**, 4312–4321.
- Y. Luo, Y. Bai, A. Mistry, Y. Zhang, D. Zhao, S. Sarkar, J. V. Handy, S. Rezaei, A. C. Chuang, L. Carrillo, K. Wiaderek, M. Pharr, K. Xie, P. P. Mukherjee, B.-X. Xu and S. Banerjee, Effect of crystallite geometries on electrochemical performance of porous intercalation electrodes by multiscale operando investigation, *Nat. Mater.*, 2022, **21**, 217–227.
- Y. Wu, G. Gao, H. Yang, W. Bi, X. Liang, Y. Zhang, G. Zhang and G. Wu, Controlled synthesis of V<sub>2</sub>O<sub>5</sub>/MWCNT core/shell hybrid aerogels through a mixed growth and self-assembly methodology for supercapacitors with high capacitance and ultralong cycle life, *J. Mater. Chem. A*, 2015, **3**, 15692–15699.
- J. Bao, X. Zhang, L. Bai, W. Bai, M. Zhou, J. Xie, M. Guan, J. Zhou and Y. Xie, All-solid-state flexible thin-film supercapacitors with high electrochemical performance based on a two-dimensional V<sub>2</sub>O<sub>5</sub>-H<sub>2</sub>O/graphene composite, *J. Mater. Chem. A*, 2014, **2**, 10876–10881.
- H. Pang, P. Cheng, H. Yang, J. Lu, C. X. Guo, G. Chang and M. Li, Template-free bottom-up synthesis of yolk-shell vanadium oxide as high-performance cathode for lithium ion batteries, *Chem. Commun.*, 2013, **49**, 1536–1538.
- E. Armstrong, M. I. Osiak, H. Geaney, C. Glynn and C. O'Dwyer, 2D and 3D vanadium oxide inverse opals and hollow sphere arrays, *CrystEngComm*, 2014, **16**, 10804–10815.
- L. Gu, J. Wang, J. Ding, B. Li and S. Yang, W-doped VO<sub>2</sub>(B) nanosheets-built 3D networks for fast lithium storage at high temperature, *Electrochim. Acta*, 2019, **295**, 393–400.



- 18 A. Jin, W. Chen, Q. Zhu, Y. Yang, V. L. Volkov and G. S. Zakharova, Structural and electrochromic properties of molybdenum doped vanadium pentoxide thin films by sol-gel and hydrothermal synthesis, *Thin Solid Films*, 2009, **517**, 2023–2028.
- 19 G. Huang, C. Li, J. Bai, X. Sun and H. Liang, Controllable-multichannel carbon nanofibers-based amorphous vanadium as binder-free and conductive-free electrode materials for supercapacitor, *Int. J. Hydrogen Energy*, 2016, **41**(47), 22144–22154.
- 20 C. Xiong, A. E. Aliev, B. Gnade and K. J. Balkus, Fabrication of Silver Vanadium Oxide and  $V_2O_5$  Nanowires for Electrochromics, *ACS Nano*, 2008, **2**, 293–301.
- 21 G. Wang, X. Lu, Y. Ling, T. Zhai, H. Wang, Y. Tong and Y. Li, LiCl/PVA Gel Electrolyte Stabilizes Vanadium Oxide Nanowire Electrodes for Pseudocapacitors, *ACS Nano*, 2012, **6**(11), 10296–10302.
- 22 A. M. Engstrom and F. M. Doyle, Exploring the cycle behavior of electrodeposited vanadium oxide electrochemical capacitor electrodes in various aqueous environment, *J. Power Sources*, 2013, **228**, 120–131.
- 23 H. Song, C. Liu, C. Zhang and G. Cao, Self-doped  $V^{4+}$ - $V_2O_5$  nanoflake for Li-ion intercalation with enhanced rate and cycling performance, *Nano Energy*, 2016, **22**, 1–10.
- 24 T. Zhai, X. Lu, Y. Ling, M. Yu, G. Wang, T. Liu, C. Liang, Y. Tong and Y. Li, A New Benchmark Capacitance for Supercapacitor Anodes by Mixed-Valence Sulfur-Doped  $V_6O_{13-x}$ , *Adv. Mater.*, 2014, **26**(33), 5869–5875.
- 25 L. Li, U. Steiner and S. Mahajan, Improved electrochromic performance in inverse opal vanadium oxide films, *J. Mater. Chem.*, 2010, **20**, 7131–7134.
- 26 H. Li, H. Djaoued, J. Robichaud and Y. Djaoued, A pleasant blue-green colored 2D Vanadium dioxide inverse opal monolayer: large area fabrication and its thermochromic application, *J. Mater. Chem. C*, 2020, **8**, 11572–11580.
- 27 H. Li, Z. Tang, Y. Liu, J. Robichaud, J. Liang, W. Jiang and Y. Djaoued, Two-Dimensional  $V_2O_5$  Inverse Opal: Fabrication and Electrochromic Application, *Materials*, 2022, **15**, 2904.
- 28 H. Zhao, Y. Meng, H. Yu, Z. Li and Z. Liu, 1D/2D  $Co_3O_4$ /NiO composite film for high electrochromic performance, *Ceram. Int.*, 2022, **48**, 32205–32212.
- 29 F. Urena-Begara, A. Crunteanu and J.-P. Raskin, Raman and XPS characterization of vanadium oxide thin films with temperature, *Appl. Surf. Sci.*, 2017, **403**, 717–727.
- 30 M. B. Sahana, C. Sudakar, C. Thapa, V. M. Naik, G. W. Auner, R. Naik and K. R. Padmanabhan, The effect of titanium on the lithium intercalation capacity of  $V_2O_5$  thin films, *Thin Solid Films*, 2009, **517**, 6642–6651.
- 31 Z.-Y. Li, C.-J. Zhou, W. Lin, Q.-H. Wu and J.-Y. Kang, Influence of intercalated Li on Electronic structures and optical properties of  $V_2O_5$ , *Chin. J. Lumin.*, 2007, **28**(1), 1–6.
- 32 G. Wu, K. Du, C. Xia, X. Kun, J. Shen, B. Zhou and J. Wang, Optical absorption edge evolution of vanadium pentoxide films during lithium intercalation, *Thin Solid Films*, 2005, **485**, 284–289.
- 33 Q. Liu, Q. Chen, Q. Zhang, G. Dong, X. Zhong, Y. Xiao, M. P. Delplancke-Ogletree, F. Reniers and X. Diao, *Electrochim. Acta*, 2018, **269**, 617–623.
- 34 C. M. Cholant, T. M. Westphal, R. D. C. Balboni, E. A. Moura, A. Gündel, W. H. Flores, A. Pawlicka and C. O. Avellaneda, Thin films of  $V_2O_5$ /MoO<sub>3</sub> and their applications in electrochromism, *J. Solid State Electrochem.*, 2017, **21**(5), 09–1515.
- 35 C. O. Avellaneda, Electrochromic performance of sol-gel deposited  $V_2O_5$ : Ta films, *Mater. Sci. Eng. B*, 2007, **138**(2), 118–122.
- 36 M. Panagopoulou, D. Vernardou, E. Koudoumas, D. Tsoukalas and Y. S. Raptis, Tungsten doping effect on  $V_2O_5$  thin film electrochromic performance, *Electrochim. Acta*, 2019, **321**, 134743.
- 37 C. E. Patil, P. R. Jadhav, N. L. Tarwal, H. P. Deshmukh, M. M. Karanjkar and P. S. Patil, Electrochromic performance of mixed  $V_2O_5$ -MoO<sub>3</sub> thin films synthesized by pulsed spray pyrolysis technique, *Mater. Chem. Phys.*, 2011, **126**(3), 711–716.
- 38 M. Ebner, D.-W. Chung, R. E. García and V. Wood, Tortuosity anisotropy in lithium-ion battery electrodes, *Adv. Energy Mater.*, 2014, **4**, 1301278.
- 39 Y.-L. Ding, Y. Wen, C. Wu, P. A. V. Aken, J. Maier and Y. Yu, 3D  $V_6O_{13}$  Nanotextiles Assembled from Interconnected Nanogrooves as Cathode Materials for high-Energy lithium ion Batteries, *Nano Lett.*, 2015, **15**, 1388–1394.
- 40 C. Zhang, Q. Yang, C. Koughia, F. Ye, M. Sanayei, S.-J. Wen and S. Kasap, Characterization of vanadium oxide thin films with different stoichiometry using Raman spectroscopy, *Thin Solid Films*, 2016, **620**, 64–69.
- 41 K. West, B. Zachau-Christiansen, T. Jacobsen and S. J. Atlung,  $V_6O_{13}$  as cathode material for lithium cells, *J. Power Sources*, 1985, **14**, 235–245.
- 42 J. Barker, E. S. Saidi and M. Y. Saidi, An investigation into the discharge capacity loss for composite insertion electrodes based on  $Li_xV_6O_{13}$ , *Electrochim. Acta*, 1995, **40**, 949–952.
- 43 N. A. Chernova, M. Roppolo, A. C. Dillon and M. S. Whittingham, Layered vanadium and molybdenum oxides: batteries and electrochromics, *J. Mater. Chem.*, 2009, **19**, 2526–2552.
- 44 H. Bjork, S. Lidin, T. Gustafsson and J. O. Thomas, Superlattice formation in the lithiated vanadium oxide phases  $Li_{0.67}V_6O_{13}$  and  $LiV_6O_{13}$ , *Acta Cryst.*, 2001, **B57**, 759–765.
- 45 P. Simon and Y. Gogotsi, Materials for electrochemical capacitors, *Nat. Mater.*, 2008, **7**(11), 845–854.
- 46 D. W. Murphy, P. A. Christian, F. J. DiSalvo, J. N. Carides and J. V. Waszczak, Lithium Incorporation by  $V_6O_{13}$  and Related Vanadium (+4, +5) Oxide Cathode Materials, *J. Electrochem. Soc.*, 1981, **128**, 2053–2059.
- 47 B. Pequenard, D. Gouried and N. Baffier, EPR identification of  $Li_xV_2O_5$  phases generated by chemical and electrochemical lithium intercalation in  $V_2O_5$ , *Solid State Ion.*, 1995, **78**, 287–303.
- 48 D. W. Murphy, P. A. Christian, F. J. DiSalvo and J. V. Waszczak, Lithium incorporation by vanadium pentoxide, *Inorg. Chem.*, 1979, **18**, 2800–2803.

- 49 J. M. Cocciantelli, J. P. Doumerc, M. Pouchard, M. Broussely and J. Labat, Crystal chemistry of electrochemically inserted  $\text{Li}_x\text{V}_2\text{O}_5$ , *J. Power Sources*, 1991, **34**, 103–111.
- 50 R. J. Cava, A. Santoro, D. W. Murphy, S. M. Zahurak, R. M. Fleming, P. Marsh and R. S. Roth, The structure of the lithium-inserted metal oxide  $\delta\text{-LiV}_2\text{O}_5$ , *J. Solid State Chem.*, 1986, **65**, 63–71.
- 51 G. Zhao, W. Wang, X. Wang, X. Xia, C. Gu and J. Tu, A multicolor electrochromic film based on a  $\text{SnO}_2/\text{V}_2\text{O}_5$  core/shell structure for adaptive camouflage, *J. Mater. Chem. C*, 2019, **7**(19), 5702–5709.
- 52 T. K. Le, P. V. Pham, C.-L. Dong, N. Bahlawane, D. Vernardou, I. Mjejri, A. Rougier and S. W. Kim, Recent advances in vanadium pentoxide ( $\text{V}_2\text{O}_5$ ) towards related applications in chromogenics and beyond: fundamentals, progress, and perspectives, *J. Mater. Chem. C*, 2022, **10**, 4019–4071.